nature nanotechnology

Article

https://doi.org/10.1038/s41565-023-01579-w

Controllable van der Waals gaps by water adsorption

Received: 16 June 2023

Accepted: 22 November 2023

Published online: 4 January 2024

Check for updates

Chang Liu[1,2,7], Xuming Zou[1,7] ✉, Yawei Lv[1,7], Xingqiang Liu[3], Chao Ma[1], Kenli Li[1], Yuan Liu[1], Yang Chai[4], Lei Liao[3,5] ✉ & Jun He[6] ✉

Van der Waals (vdW) gaps with ångström-scale heights can confine molecules or ions to an ultimately small scale, providing an alternative way to tune material properties and explore microscopic phenomena. Modulation of the height of vdW gaps between two-dimensional (2D) materials is challenging due to the vdW interaction. Here we report a general approach to control the vdW gap by preadsorption of water molecules on the material surface. By controlling the saturation vapour pressure of water vapour, we can precisely control the adsorption level of water molecules and vary the height of the vdW gaps of MoS_2 homojunctions from 5.5 Å to 53.6 Å. This technique can be further applied to other homo- and heterojunctions, constructing controlled vdW gaps in 2D artificial superlattices and in 2D/3D and 3D/3D heterojunctions. Engineering the vdW gap has great practical potential to modulate the device performance, as evidenced by the vdW-gap-dependent diode characteristics of the MoS_2/gap/MoS_2 junction. Our work introduces a general strategy of molecular preadsorption that can extend to various precursors, creating more tunability and variability in vdW material systems.

The development of van der Waals (vdW) integration offers tremendous flexibility for mixing and matching of distinct two-dimensional (2D) crystals beyond the limits of lattice-matching requirements to create various vdW heterostructures and artificial superlattices[1–4]. As a derivative of vdW technology, vdW gaps with ångström-scale heights have recently become a topic of special interest. First, manipulating vdW gaps can effectively tune the interlayer distances, phase compositions, and electronic and optical properties of 2D materials[5–8]. Second, designing vdW gaps in vdW structures makes it possible to obtain various functional devices with customized performance[9]; for example, constructing a vdW gap between dielectric and channel can decouple their interaction and preserve the intrinsic properties of the channel[10]. Moreover, ångström-scale gaps have been recognized as the most useful tool for studying exotic phenomena at the ultimately small scale of materials science[11], especially the size of single or several atoms and molecules, such as capillary condensation[12], 'ballistic' gas transport[13,14], mutant dielectric features[15], etc. In addition, extremely small vdW gaps (subnanometre), with heights that can be less than the diameter of the smallest hydrated ions, can be used as a kind of selective permeation pore, and have great application potential in water filtration, molecular/ion separation and desalination[16–19]. However, creating vdW gaps at the nanoscale has been a technical challenge. Once the vdW interaction is established, it is difficult to change the height of the vdW gaps because this dimension mainly depends on the lowest potential of the vdW interaction and the intrinsic properties of the atoms involved[1,2]. So far, the strategies for opening such gaps have

[1]Key Laboratory for Micro/Nano Optoelectronic Devices of Ministry of Education & Hunan Provincial Key Laboratory of Low-Dimensional Structural Physics and Devices, School of Physics and Electronics, Hunan University, Changsha, China. [2]State Key Laboratory of Infrared Physics, Shanghai Institute of Technical Physics, Chinese Academy of Sciences, Shanghai, China. [3]State Key Laboratory for Chemo/Biosensing and Chemometrics, College of Semiconductors (College of Integrated Circuits), Hunan University, Changsha, China. [4]Department of Applied Physics, The Hong Kong Polytechnic University, Hong Kong, China. [5]School of Physics and Electronic Engineering, Harbin Normal University, Harbin, China. [6]Key Laboratory of Artificial Micro- and Nano-structures of Ministry of Education and School of Physics and Technology, Wuhan University, Wuhan, China. [7]These authors contributed equally: Chang Liu, Xuming Zou, Yawei Lv. ✉e-mail: zouxuming@hnu.edu.cn; liaolei@whu.edu.cn; he-jun@whu.edu.cn

https://doi.org/10.1038/s41565-023-01579-w

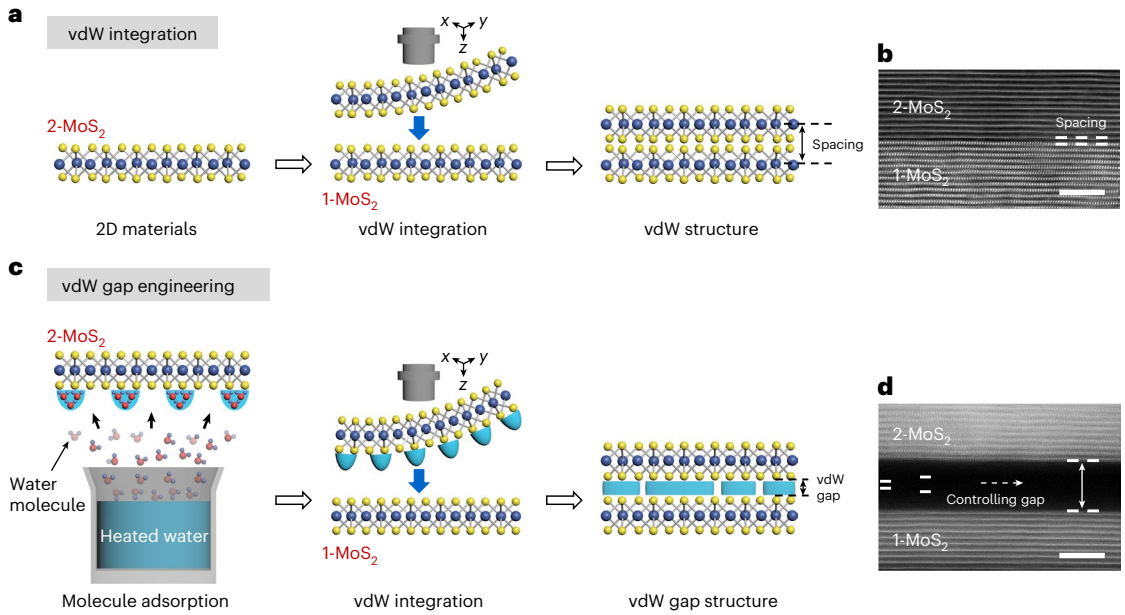

Fig. 1 | Illustration and structural characterizations of conventional vdW integration and vdW gap engineering. a, Schematic illustrations of a typical vdW integration with MoS_2 homojunction as an example. **b**, Cross-sectional STEM image of the vdW interface formed by vdW integration; here the 1-MoS_2 and 2-MoS_2 layers are assembled into a new MoS_2 layer with a neat layered feature. **c**, Schematic illustrations of the vdW gap engineering achieved by adsorption of water molecules, where water molecules are preadsorbed on the material surface by heating ultrapure water to produce saturated water vapour. The 2-MoS_2 preabsorbs water molecules and further assembles vdW structures with a clean 1-MoS_2 to create the vdW gap. **d**, Cross-sectional STEM image of the vdW interface formed by vdW gap engineering, showing a clear vdW gap while maintaining atomically sharp and clean interfaces. Scale bars, 5 nm (**b**,**d**).

relied only on electrochemical intercalation techniques[20–25], in which guest particles are forcibly inserted between the vdW layers of the host material. However, the introduction of certain organic macromolecules (for example, cetyl-trimethylammonium bromide) or alkali metal ions (for example, Li^+, Na^+) drastically alters the electronic properties of the host materials while resulting in poor stability. In addition, this method offers insufficient control over the height of vdW gaps and can only be applied to specific material systems[20,23]. Although some embryonic concepts and interesting science relating to vdW gaps have been reported[10,12–16,26,27], no universal approach for opening and controlling vdW gaps appears to exist.

In this work, we report a straightforward approach to control vdW gaps by preadsorption of water molecules on a material surface and subsequently assembling the vdW structures. In a home-designed apparatus, we can precisely control the level of water molecule adsorption by varying the saturated vapour pressure (SVP) of water vapour and achieve the opening and varying of vdW gaps on the ångström-scale. Using 2D MoS_2 as a representative material, we reveal the dynamic evolution of the adsorption of water molecules on the MoS_2 surface with increasing SVP, and show a monotonic increase in the vdW gap height (h_{vdW}) of a MoS_2 homojunction from 5.5 Å to 53.6 Å. Scanning transmission electron microscopy (STEM) studies demonstrate that the vdW water gaps thus created have atomically flat and clean interfaces at different h_{vdW}. Importantly, this gap engineering is capable of extending to all 2D systems, and even to 3D systems, and the adsorption precursors can also be extended to different solutions to form various molecule or ion gaps. We further demonstrate that this gap engineering has great potential for functional devices. For example, density functional theory (DFT) calculations show that water molecules spontaneously polarize on the MoS_2 surface and induce an orderly polarization arrangement of subsequent water molecules. The great vertical polariton-potential-difference (PPD) induced by the polarized water layer allows the MoS_2/gap/MoS_2 homo-gap-junction (MoS_2 HOGJ) to exhibit gap-dependent diode characteristics with an ideal factor of 1 and an ultrahigh rectification ratio of $>10^5$, together with superior stability.

Van der Waals gap engineering

Schematic process flows and comparisons of conventional vdW integration and our vdW gap engineering are shown in Fig. 1. Using 2D MoS_2 crystal as a model, conventional vdW integration involves physically laminating one MoS_2 directly onto another MoS_2 to form an MoS_2 homojunction (Fig. 1a and Methods). A STEM image of a vdW interface formed by conventional vdW integration is shown in Fig. 1b, where the entire homojunction appears as an intact thicker MoS_2 crystal with a neat layered structure. Except for crystal orientation differences when stacking, no special features are observed at the vdW interface of two MoS_2 layers, and the interface has the same layer spacing of about 6.2 Å as a normal MoS_2 layer. Note that the layer spacing is different from the vdW gap[2], and for 2D MoS_2 crystals, the intrinsic layer spacing and vdW gap are 6.2 Å and 1.8 Å, respectively (Supplementary Fig. 1). In contrast to conventional vdW integration, the vdW gap engineering we report emphasizes the preadsorption of water molecules onto the material prior to integration, and then physical assembly to form a vdW water gap structure (Fig. 1c and Methods). Here, we first place an MoS_2 under a specific SVP for a fixed time adsorption. After that, this MoS_2 is rapidly laminated to another, and the preadsorbed water can be rapidly squeezed by the flat upper/lower MoS_2 and stably confined between the two MoS_2 layers, supporting a vdW gap filled with water molecules. The gap heights can be precisely controlled by varying the SVP. The interface features of MoS_2 homojunction fabricated by vdW gap engineering are shown in Fig. 1d. Here, an atomically flat and clean vdW gap was formed between the 1-MoS_2 and 2-MoS_2 interface, which uniformly decoupled the vdW interactions between the two MoS_2 layers. Moreover, the natural adsorption of 'low-energy' water molecules caused no damage to the MoS_2 layers, which still feature an atomically sharp and clean interface.

Molecule adsorption and controlled vdW gaps

The microscopic features of water molecule adsorption and the structural characterizations of controllable vdW gaps are demonstrated in Fig. 2. We used atomic force microscopy (AFM) to reveal the evolution

https://doi.org/10.1038/s41565-023-01579-w

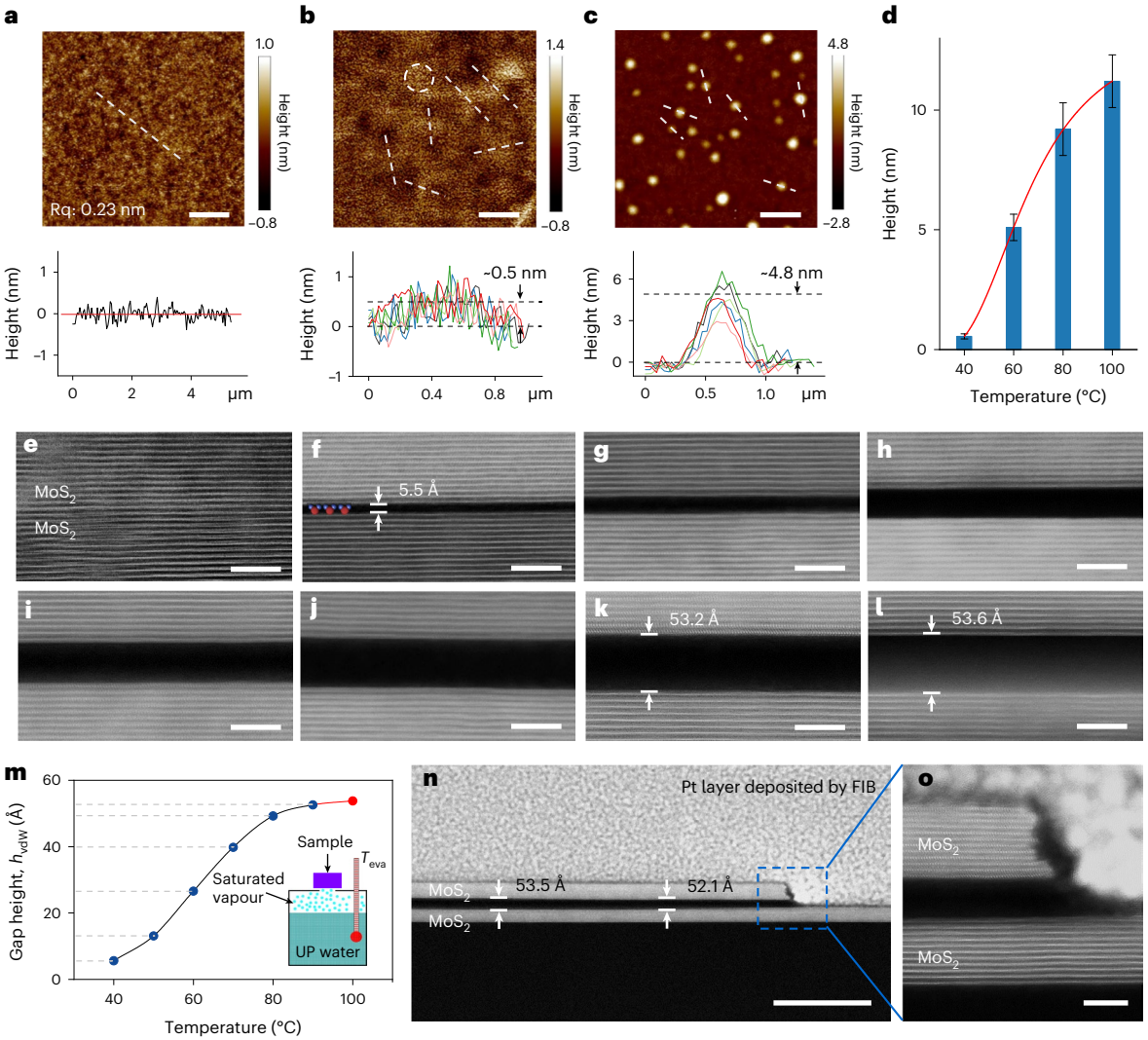

Fig. 2 | Dynamic evolutions of water molecule adsorption and structural characterizations of controllable vdW gaps. a–**c**, Upper panels: AFM images of MoS_2 surfaces under different adsorption levels and height profiles of water islands corresponding to no vapour (**a**), 40 °C (**b**) and 60 °C (**c**). Rq, r.m.s. roughness. The dashed circle region (upper panel of (**b**)) shows a typical island-like water adlayer. The height profiles along the dashed lines (upper panels of (**a**–**c**)) are displayed in their lower panels. Lower panels: all x-axis labels are defined as plane position dimensions being measured. The different colour graphs associated with the dashed lines need not be precisely distinguished and are only intended to show the average height of the water islands. **d**, Average height of water islands on the MoS_2 surface at different adsorption levels. The error bars represent the s.d. of the same sets. **e**, STEM image of the MoS_2 homojunction vdW interface without the involvement of water molecules. **f**–**l**, A series of STEM images showing the vdW gap height increasing monotonically with SVP: 40°C (**f**), 50°C (**g**), 60°C (**h**), 70°C (**i**), 80°C (**j**), 90°C (**k**), 100°C (**l**). **m**, Extracted gap height h_{vdW} as a function of temperature. UP, ultrapure. **n**, Edge characteristics of a vdW gap at maximum height, where the gap height remains uniform over a wide range and does not collapse at the edge of the gap. **o**, High-magnification STEM images of edge features of the vdW gap. Scale bars, 2 μm (**a**–**c**), 5 nm (**e**–**l**,**o**), 50 nm (**n**).

of the adsorption of water molecules on the MoS_2 surface under different SVPs. The SVP was controlled by simply changing the evaporation temperature (T_{eva}, °C) of ultrapure water in a home-designed apparatus (Extended Data Fig. 1 and Methods). The pristine MoS_2 exhibits uniform surface characteristics with low roughness of ~0.23 nm (Fig. 2a). After 10 min of water adsorption under 40 °C SVP, some island-like adlayers appear on the MoS_2 surface (dashed circle), and the height profile indicates an average height of ~0.5 nm (Fig. 2b). With increasing temperature, the islands gradually increase until they reach an average height of ~11.2 nm under 100 °C (Fig. 2c and Extended Data Fig. 2). The greater the number of surface defects, the more water islands appeared on the surface of the MoS_2 (Supplementary Fig. 2). We carried out Raman, photoluminescence (PL) and X-ray photoelectron spectroscopy (XPS) characterizations to demonstrate that the interaction between water molecules and 2D materials is physisorption (Supplementary Fig. 3 and Supplementary Note 1). The DFT calculations show that water molecules have higher binding energy at a sulfur-vacancy defect site (~209.6 meV) than at a defect-free site (~148.2 meV), and thus are more likely to cluster near defects to form a large droplet (Extended Data Fig. 3, Supplementary Discussion 1 and Extended Data Fig. 4d). As T_{eva} increases, the higher SVP allows more energetic water molecules to form higher water islands around the defect sites. Note that when the water islands transition from the molecular scale to the nanoscale, their size is likely to be related to the hydrophilicity of the material, which will be another major factor affecting the growth of the water islands. When this adsorption is complete, the preadsorbed MoS_2 is quickly laminated to another clean piece of MoS_2, making the water islands form an atomically flat vdW water gap (see Methods for details). Thus, the vdW gap height is greatly dependent on the height of the water island. We recorded the heights of the water islands at different T_{eva} and found that they exhibit a monotonic increase with temperature (Fig. 2d).

https://doi.org/10.1038/s41565-023-01579-w

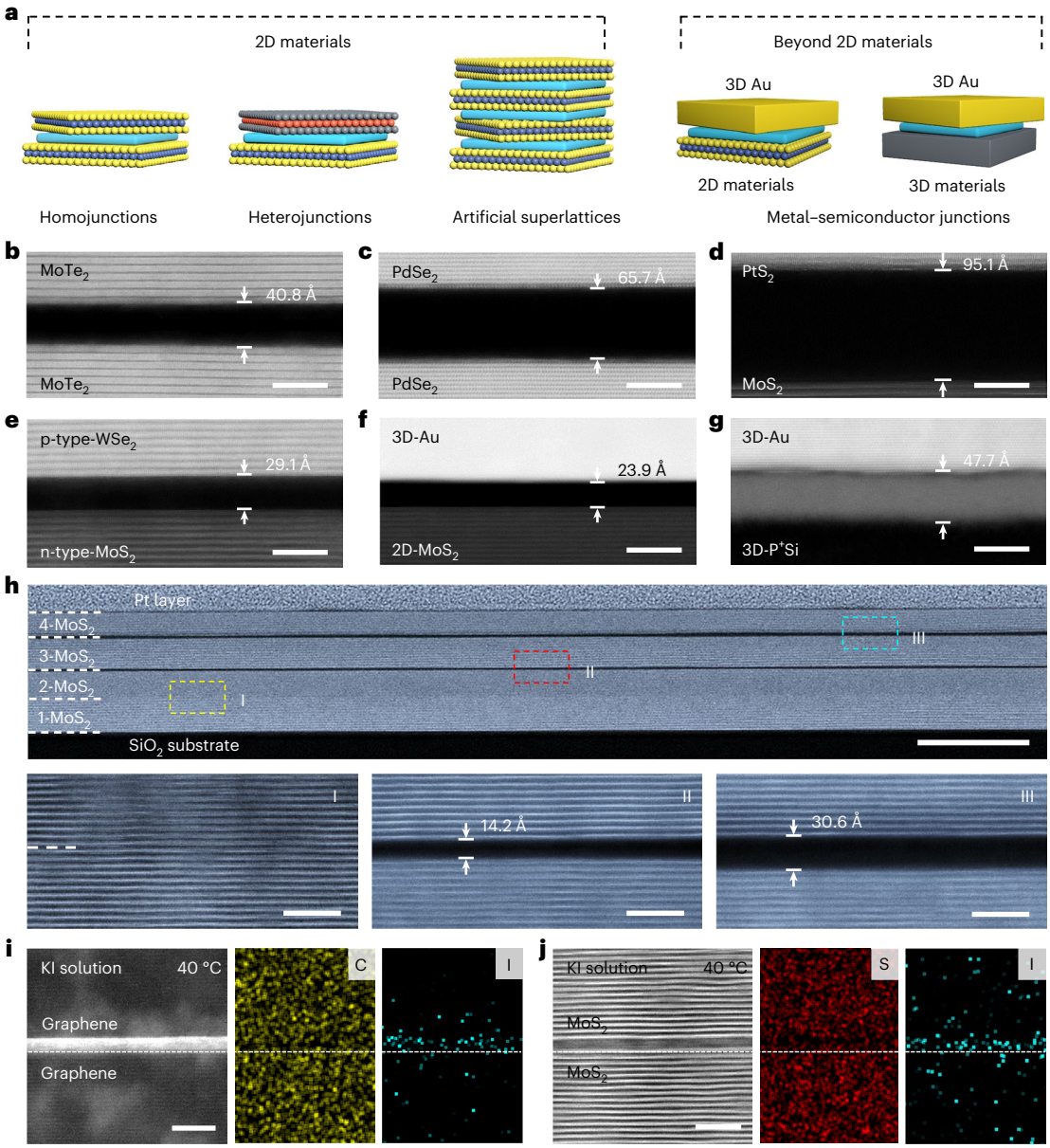

Fig. 3 | Extendable material systems, realizable superlattice concepts and extendable adsorption precursors of vdW gap engineering. **a**, Expandable systems for vdW gap engineering, including 2D/2D homojunctions, 2D/2D heterojunctions, 2D artificial superlattices, and 2D/3D and 3D/3D heterojunctions. **b**–**g**, Selected STEM images of vdW gaps in 2D/2D homojunctions ($MoTe_2$/gap/$MoTe_2$ (**b**) and $PdSe_2$/gap/$PdSe_2$ (**c**)), 2D/2D heterojunctions (PtS_2/gap/MoS_2 (**d**) and p-type-WSe_2/gap/n-type-MoS_2 (**e**)) and 3D systems (3D-Au/gap/2D-MoS_2 (**f**) and 3D-Au/gap/3D-P^+Si (**g**)), showing the multisystem and multidimensional applicability of the gap engineering. **h**, Upper panel: artificial superlattice concept with highly controlled vdW gaps using MoS_2 as a model. Lower panels: vdW interfaces corresponding to MoS_2 layers 1/2 (I), 2/3 (II) and 3/4 (III). **i**,**j**, STEM images and elemental analysis of the vdW KI gap produced by choosing KI solution as the adsorption precursor for graphene/KI-gap/graphene (**i**) and MoS_2/KI-gap/MoS_2 (**j**), indicating that our gap engineering approach is expandable to different precursors. Scale bars, 5 nm (**b**–**g**, **h** (lower), **i**,**j**), 100 nm (**h**)(upper)).

The controllability of molecule-adsorption-induced vdW gaps is further verified by STEM (Fig. 2e–i), indicating a series of gap heights that monotonically increase with SVP. When no water molecules are introduced (assembled in a nitrogen-filled glovebox), the MoS_2 homojunction appears as a thicker MoS_2 atomic crystal (Fig. 2e). With a T_{eva} of 40 °C, the MoS_2 homojunction starts to show a vdW gap with h_{vdW} = 5.5 Å (Fig. 2f). As T_{eva} increases (at 10 °C intervals), h_{vdW} also increases steadily until it reaches a maximum of ~53.2 Å at 90 °C (Fig. 2g–k). When T_{eva} further rises to 100 °C, the gap height hardly increases further (Fig. 2l), at which point the adsorption of MoS_2 has reached saturation. We extract h_{vdW} as a function of temperature plotted in Fig. 2m, and find that it increases monotonically with temperature until saturation. This demonstrates the possibility of precise control of h_{vdW} at the ångström scale by simply adjusting the evaporation temperature. To verify the wide range of uniformity and edge characteristics of the vdW gaps, STEM characterization of a MoS_2 HOGJ with maximum h_{vdW} is performed, where the vdW gap maintains a uniform height over a wide range and remains stable at the gap edge without collapsing (Fig. 2n,o). Here, all of the above gap structures were assembled using multilayer MoS_2. Because the mechanical hardness of multilayer materials is higher than that of single layer, the droplets can be squeezed. This allows different-sized droplets to support and form a uniform height gap, in which water and empty spaces alternate (Extended Data Fig. 4 and Supplementary Discussion 2). Meanwhile, Raman, STEM and AFM analyses were employed to investigate the thermal stability (30–250 °C) of the vdW gap (Supplementary Fig. 4,

https://doi.org/10.1038/s41565-023-01579-w

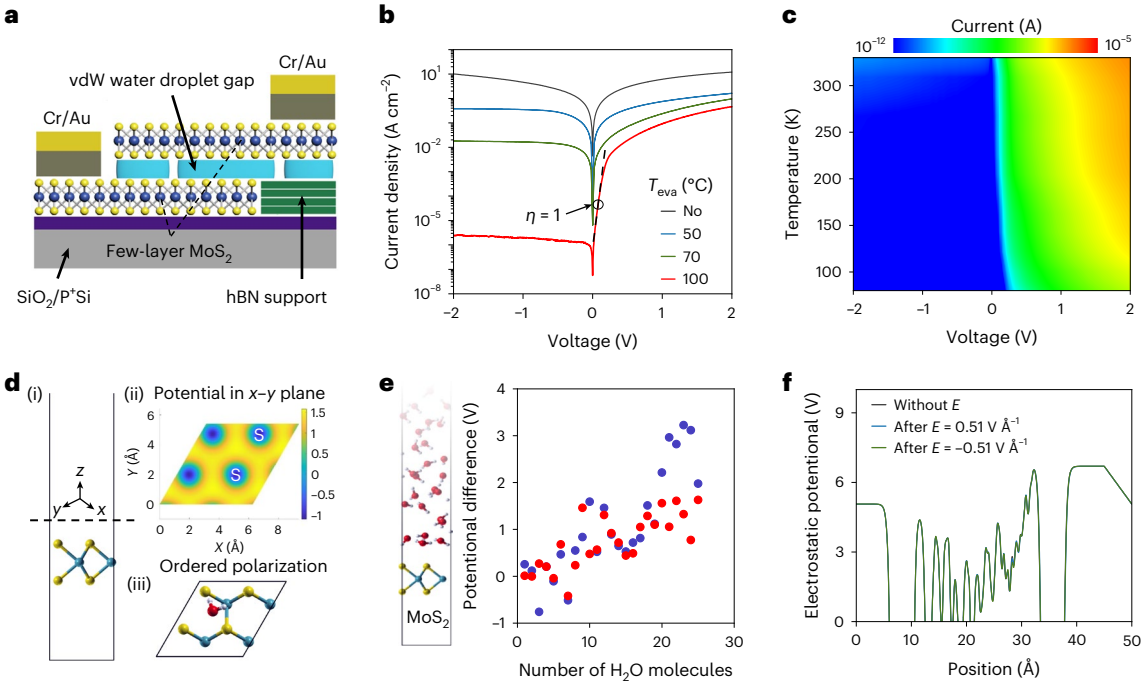

Fig. 4 | Electrical properties of MoS_2/gap/MoS_2 junction and DFT calculations. **a**, Schematic illustration of MoS_2/gap/MoS_2 junction with two electrodes deposited on MoS_2. **b**, The normalized *I*–*V* curves show the rectification characteristics of the MoS_2/gap/MoS_2 junction at different gap heights (including no gap and gaps induced by varying the SVP (50, 70, and 100 °C)), where 100 °C realizes the best rectification characteristic with a perfect ideal factor (η) of 1. **c**, Temperature-dependent *I*–*V* characteristics, showing that the device can maintain good rectification characteristics in the temperature range 80–330 K. **d**, The 2 × 2 MoS_2 supercell model and the in-plane potential on its top (black dotted line) where the first H_2O molecule will locate, showing a large in-plane potential difference of 2.5 V which is sufficient to guide in an orderly fashion the polarizations of the first few approaching H_2O molecules. For example, the stacking of the first H_2O molecule is shown and the polarization direction is in-plane. Along the stacking, the potentials felt by the following H_2O molecules are varied and the vertical polarization begins. **e**, PPD in the vertical direction of the MoS_2/H_2O (blue dots) and $MoS_2/H_2O/MoS_2$ (red dots) structures, with increasing number of H_2O molecules; here both structures remain consistent. **f**, Stability of the polarization potential of the $MoS_2/H_2O/MoS_2$ structure under an external electric field, where the applied electric field has little effect on the potential difference of the system. *E*, applied electric field.

Supplementary Note 2, Extended Data Fig. 5 and Supplementary Discussion 3). The results show that the vdW gap remains stable upon 90 °C annealing. At higher annealing temperatures (>90 °C), the gap edge gradually collapses, thus encasing the water inside and preventing it from further volatilizing (Extended Data Fig. 5a–c). We have confirmed that when the vdW gap is encapsulated with few-layer hexagonal BN (hBN), it can remain stable at an annealing temperature of 250 °C (Extended Data Fig. 5d,e). In addition, the gap height can remain unchanged for up to 1 month at room temperature, further confirming the excellent environmental stability (Supplementary Fig. 5).

Water molecule adsorption can be extended to a variety of materials, and therefore vdW gap engineering is universal to all 2D materials, making it possible to form gap-controlled 2D/2D homojunctions, 2D/2D heterojunctions, 2D artificial superlattices, etc., and even beyond 2D materials to include 2D/3D and 3D/3D heterojunctions, hence covering almost every kind of heterointerface (Fig. 3a). Notably, due to differences in defect density and hydrophilicity, different materials have different adsorption capacities under the same SVP, and therefore have different h_{vdW} when integrated with other materials. To verify this feature, three different materials (WS_2, MoS_2 and PtS_2) were selected for water molecule adsorption at T_{eva} = 100 °C, and subsequently assembled into gap structures with standard MoS_2 (Supplementary Fig. 6). The surface water island heights of WS_2, MoS_2 and PtS_2 by AFM analysis are 4.1, 11.2 and 24.5 nm, respectively, and the h_{vdW} of the corresponding WS_2/gap/MoS_2, MoS_2/gap/MoS_2 and PtS_2/gap/MoS_2 junctions are 21.5, 53.6 and 95.1 Å, which indicates that the gap heights are heavily dependent on the amount of the preadsorbed water. We have demonstrated a variety of vdW gap structures using different materials as adsorption and combination objects, including 2D/2D homojunctions (such as graphene/graphene, $PdSe_2/PdSe_2$, $MoTe_2/MoTe_2$ and ReS_2/ReS_2), 2D/2D heterojunctions including p–n junctions and semimetal–semiconductor junctions (such as WS_2/MoS_2, PtS_2/MoS_2, ReS_2/MoS_2, WSe_2/MoS_2 and $PdSe_2/MoS_2$) and 2D/3D and 3D/3D metal–semiconductor junctions (such as Au/MoS_2 and Au/P^+Si) (Fig. 3b–g and Extended Data Fig. 6). Here, the gaps remain uniform over a large range regardless of the material groups, ruling out material strain and demonstrating the feasibility of vdW gap engineering (Extended Data Fig. 7). Meanwhile, we performed energy-dispersive spectrometry (EDS) elemental analyses to investigate the gap compositions (Extended Data Fig. 8), and found that elemental silicon was detected in all gaps. During the focused ion beam (FIB) milling process, the redeposited silicon and its oxides can fill the original gaps, which is equivalent to a 3D in situ encapsulation on both sides of the water gap, further supporting the above cross-sectional slices which do not collapse even at gaps up to ~10 nm, while also enabling stable imaging (Supplementary Fig. 7). Note that the redeposition process did not cause measurement errors in the gap sizes. The AFM images of the sample edges show that the gap height is ~5.3 nm (MoS_2 at T_{eva} = 100 °C) prior to the FIB process (Extended Data Fig. 5), which is consistent with the corresponding cross-section STEM-measured height of 5.36 nm (Fig. 2l). Here, Raman spectroscopy was used to confirm the presence of water in the vdW gaps (see Supplementary Fig. 8 and Supplementary Note 3 for details).

In addition, the vdW gap engineering makes it possible for multiple alternating laminations to form complex artificial superlattices. In Fig. 3h, we use MoS_2 as a model and demonstrate a new concept for preparing artificial superlattices, where the height of the vdW gap between the MoS_2 multilayers is freely controlled and assembled (from none to existent and increasing). We show a four-layer stacked

MoS_2 vdW structure with no gap present between layers 1 and 2, a 14.2 Å gap between layers 2 and 3, and a 30.6 Å gap between layers 3 and 4. All gaps are highly uniform in the range of a few micrometres, while multiple molecular adsorptions and stackings do not break the vdW layer-to-layer interface (Supplementary Fig. 9). Importantly, the gap engineering is not only applicable to water solutions, but can also be extended to other ionic solutions. We changed the ultrapure water to KI solution and used the same apparatus to obtain saturated vapour for hydrated ion adsorption. STEM images and elemental analysis show that the vdW KI solution gaps (KI-gaps) in graphene (Fig. 3i) and MoS_2 (Fig. 3j) homojunction are filled with iodide ions (the element intensity of the line scan is displayed in Supplementary Fig. 10), while the adsorption process caused no damage to the material. Compared to using complex electrochemical intercalation to produce ion gaps, our gap engineering, which creates ion gaps by simply changing the adsorptive ionic solution, has greater controllability and versatility, and is an attractive method for regulating superconductivity[28], thermoelectricity[29] or spin-polarization[30] of the resulting materials.

Gap engineering for functional devices

The vdW structures with tailored vdW gaps define a new material platform, which offers possibilities for exploring a variety of new functional devices. Here, we experimentally fabricated a MoS_2 HOGJ to evaluate the electrical characteristics, as schematically illustrated in Fig. 4a. Here, a varying-height gap is sandwiched between two ~8–10 nm MoS_2 layers and two terminal electrodes are deposited to test the current–voltage (I–V) characteristics. When there is no water gap, the MoS_2/MoS_2 junction exhibits a linear I–V curve with a high current density of 10.2 A cm^{-2} (Fig. 4b and Supplementary Fig. 11). With the introduction of the water gap, MoS_2 HOGJ exhibits a gap-dependent diode characteristic, where the rectification ratio increases with the height of the gap. At the highest water gap (53.3 Å for T_{eva} = 100 °C), this junction can exhibit an ultrahigh rectification ratio of $>10^5$, and an ideal factor of 1. Importantly, the electrical properties of the MoS_2 HOGJ diode are extremely stable. Over a period of up to 6 months, the turn-on voltage and on/off current remain almost constant (Supplementary Fig. 12), while maintaining good rectification characteristics in the 80–330 K temperature range (Fig. 4c).

We further explored the intrinsic mechanism of water-gap-induced diodes by DFT calculations. As shown in Fig. 4d, we created a 2 × 2 MoS_2 supercell model and calculated the x–y plane potential on its top at a distance of 1.24 Å from the sulfur atom (Fig. 4d-i), where the potential is lowest on the top of sulfur atom and highest at the sulfur–sulfur gaps, exhibiting a potential difference of ~2.5 V (Fig. 4d-ii). Such a large potential difference is sufficient to guide in an orderly fashion the polarization directions of the first few approaching H_2O molecules. When we place the first H_2O molecule on the MoS_2 surface and consider the dipole correction, its positively charged hydrogen atom is first attracted to the potential well on the top of the sulfur atom, while the oxygen atom is repelled, resulting in an in-plane polarization direction (Fig. 4d-iii). Meanwhile, when the second, third and subsequent H_2O molecules approach the MoS_2 surface, their polarization direction will be guided by the mixing potential fields of the MoS_2 and the previous H_2O molecules. As the number of water molecules continues to increase, they start to show a vertical polarization behaviour (blue dots in Fig. 4e). When about 25 H_2O molecules are stacked on the MoS_2 supercell surface, the vertical PPD can already exceed 3 V. Theoretically, the PPD increases without limit with the number of H_2O molecules. To fit the experimental MoS_2/H_2O/MoS_2 structure, we introduced another MoS_2 on the MoS_2/H_2O model (red dots in Fig. 4e), and found that at low H_2O layer thickness, the vertical PPD remains consistent with MoS_2/H_2O, while at high H_2O layer thickness, we noticed that the increase in the potential difference was slowed down and reached a limit value of ~1.6 V. This limitation can be explained by interlayer charge transfer between the two MoS_2 layers, which prevents the further increase of the PPD (Supplementary Fig. 13 and Supplementary Note 4). Although it is growing slowly, such a potential difference is already the largest value between MoS_2 interlayers, which is sufficient to affect the carrier transport between MoS_2 layers. Therefore, the large vertical PPD between two MoS_2 layers caused by the ordered polarization of H_2O molecules is responsible for the diode characteristics of MoS_2 HOGJ devices. This also allows us to consider the water reported here as 'nanoconfined water', as previously reported[11,14,26,31–34], which is different from 'bulk water'.

Because large water droplets are more likely to form at defect sites, we also simulated the properties of water at sulfur-vacancy defects and analysed their effects on polarization. We found that sulfur vacancies can lead to the accumulation of positive potentials on the MoS_2 surface, which is beneficial to guide the orientations of H–O bonds and enhances the polarization effect (Extended Data Fig. 9 and Supplementary Discussion 4). Compared to the defect-free MoS_2, the PPD in sulfur-vacancy models can rapidly reach ~3 V with a small amount of adsorbed water molecules. Meanwhile, we investigated the stability of the polarization orientation of H_2O molecules in the MoS_2 HOGJ system (Fig. 4f). Here, the microscopic potential in the vertical direction of the system can perfectly recover to the initial state after applying a high electric field, which demonstrates the stability of the PPD and the feasibility of applying it to modulate carrier transport. This result is also consistent with our electrical tests (Supplementary Fig. 14), and even when we change the voltage range and scan speed, the device maintains uniform I–V characteristics and has almost no hysteresis, further demonstrating that the rectification characteristics of the MoS_2 HOGJ are reliable and stable.

In addition, the rectifier characteristics of the MoS_2 HOGJ diode can be eliminated by adding KI. The DFT calculations show that embedding K^+ can affect the electric field direction and water molecule orientation, resulting in the water–K^+ system no longer exhibiting a polarized electric field and PPD (Supplementary Fig. 15 and Supplementary Note 5). Additionally, we confirm that the MoS_2 HOGJ with an ~5.3 nm gap has great potential for pressure sensing (see Extended Data Fig. 10, Supplementary Discussion 5, Supplementary Fig. 16 and Supplementary Note 6 for details). Here, the minimum detection pressure of the device is as low as 0.03 Pa, which is an order of magnitude lower than that of reported suspended-gate transistor[35], and the average sensitivity is ~3.9×10^3 kPa^{-1}, which is 1–3 orders of magnitude higher than a reported air-gap-gate MoS_2 transistor[36] and a gold-nanowire-assembled device[37]. Meanwhile, the device also shows good stability and excellent signal recognition capabilities, such as repetitive tracking of music and precise resolution of human speech.

Conclusions

We have developed a straightforward and general approach to create and control vdW gaps by preadsorption of water molecules on a material surface and further vdW integration. By controlling the adsorption of water molecules, the height of the vdW water gap can be precisely controlled at the ångström-scale, and the water gap can maintain superior stability. Meanwhile, we show that this gap engineering can be applied to other 2D systems, and even to 3D systems, and the gaps can also be filled with different molecules and ions. This provides considerable freedom to tailor the interlayer coupling, conductivity, chirality and topology of 2D materials, and is an ideal tool to study the transport properties of molecules and ions at the extreme 2D scale. Furthermore, we fabricated an ideal MoS_2/gap/MoS_2 diode to demonstrate the potential of vdW gaps for modulating carrier transport, and the proposed gap engineering can also be applied to various vdW interfaces such as semiconductor/semiconductor, dielectric/semiconductor and metal/semiconductor to tailor the performance and functionality of the devices.

Online content

Any methods, additional references, Nature Portfolio reporting summaries, source data, extended data, supplementary information, acknowledgements, peer review information; details of author contributions and competing interests; and statements of data and code availability are available at https://doi.org/10.1038/s41565-023-01579-w.

References

1. Geim, A. K. & Grigorieva, I. V. Van der Waals heterostructures. *Nature* **499**, 419–425 (2013).
2. Liu, Y., Huang, Y. & Duan, X. Van der Waals integration before and beyond two-dimensional materials. *Nature* **567**, 323–333 (2019).
3. Huang, X. et al. Recent progress on fabrication and flat-band physics in 2D transition metal dichalcogenides moiré superlattices. *J. Semicond.* **44**, 011901 (2023).
4. Novoselov, K. S. et al. Two-dimensional atomic crystals. *Proc. Natl Acad. Sci. USA* **102**, 10451–10453 (2005).
5. Qian, Q. et al. Chiral molecular intercalation superlattices. *Nature* **606**, 902–908 (2022).
6. Wu, Y., Li, D., Wu, C.-L., Hwang, H. Y. & Cui, Y. Electrostatic gating and intercalation in 2D materials. *Nat. Rev. Mater.* **8**, 41–53 (2023).
7. Zhao, X. et al. Engineering covalently bonded 2D layered materials by self-intercalation. *Nature* **581**, 171–177 (2020).
8. Yang, C. et al. Aqueous Li-ion battery enabled by halogen conversion–intercalation chemistry in graphite. *Nature* **569**, 245–250 (2019).
9. Li, Z. et al. Intercalation strategy in 2D materials for electronics and optoelectronics. *Small Methods* **5**, 2100567 (2021).
10. Luo, P. et al. Molybdenum disulfide transistors with enlarged van der Waals gaps at their dielectric interface via oxygen accumulation. *Nat. Electron.* **5**, 849–858 (2022).
11. Geim, A. K. Exploring two-dimensional empty space. *Nano Lett.* **21**, 6356–6358 (2021).
12. Yang, Q. et al. Capillary condensation under atomic-scale confinement. *Nature* **588**, 250–253 (2020).
13. Keerthi, A. et al. Ballistic molecular transport through two-dimensional channels. *Nature* **558**, 420–424 (2018).
14. Radha, B. et al. Molecular transport through capillaries made with atomic-scale precision. *Nature* **538**, 222–225 (2016).
15. Fumagalli, L. et al. Anomalously low dielectric constant of confined water. *Science* **360**, 1339–1342 (2018).
16. Gopinadhan, K. et al. Complete steric exclusion of ions and proton transport through confined monolayer water. *Science* **363**, 145–148 (2019).
17. Yang, Y. et al. Large-area graphene-nanomesh/carbon-nanotube hybrid membranes for ionic and molecular nanofiltration. *Science* **364**, 1057–1062 (2019).
18. Chen, L. et al. Ion sieving in graphene oxide membranes via cationic control of interlayer spacing. *Nature* **550**, 380–383 (2017).
19. Abraham, J. et al. Tunable sieving of ions using graphene oxide membranes. *Nat. Nanotechnol.* **12**, 546–550 (2017).
20. Rajapakse, M. et al. Intercalation as a versatile tool for fabrication, property tuning, and phase transitions in 2D materials. *NPJ 2D Mater. Appl.* **5**, 30 (2021).
21. Yu, Y. et al. Gate-tunable phase transitions in thin flakes of 1T-TaS_2. *Nat. Nanotechnol.* **10**, 270–276 (2015).
22. Xiong, F. et al. Li intercalation in MoS_2: in situ observation of its dynamics and tuning optical and electrical properties. *Nano Lett.* **15**, 6777–6784 (2015).
23. Wang, C. et al. Monolayer atomic crystal molecular superlattices. *Nature* **555**, 231–236 (2018).
24. Li, Y., Yan, H., Xu, B., Zhen, L. & Xu, C.-Y. Electrochemical intercalation in atomically thin van der Waals materials for structural phase transition and device applications. *Adv. Mater.* **33**, 2000581 (2021).
25. Bao, W. et al. Approaching the limits of transparency and conductivity in graphitic materials through lithium intercalation. *Nat. Commun.* **5**, 4224 (2014).
26. Muñoz-Santiburcio, D. & Marx, D. Confinement-controlled aqueous chemistry within nanometric slit pores. *Chem. Rev.* **121**, 6293–6320 (2021).
27. Esfandiar, A. et al. Size effect in ion transport through angstrom-scale slits. *Science* **358**, 511–513 (2017).
28. Kanetani, K. et al. Ca intercalated bilayer graphene as a thinnest limit of superconducting C_6Ca. *Proc. Natl Acad. Sci. USA* **109**, 19610–19613 (2012).
29. Wan, C. et al. Flexible n-type thermoelectric materials by organic intercalation of layered transition metal dichalcogenide TiS_2. *Nat. Mater.* **14**, 622–627 (2015).
30. Friend, R. H. & Yoffe, A. D. Electronic properties of intercalation complexes of the transition metal dichalcogenides. *Adv. Phys.* **36**, 1–94 (1987).
31. Ruiz-Barragan, S., Muñoz-Santiburcio, D. & Marx, D. Nanoconfined water within graphene slit pores adopts distinct confinement-dependent regimes. *J. Phys. Chem. Lett.* **10**, 329–334 (2019).
32. Muñoz-Santiburcio, D., Wittekindt, C. & Marx, D. Nanoconfinement effects on hydrated excess protons in layered materials. *Nat. Commun.* **4**, 2349 (2013).
33. Muñoz-Santiburcio, D. & Marx, D. On the complex structural diffusion of proton holes in nanoconfined alkaline solutions within slit pores. *Nat. Commun.* **7**, 12625 (2016).
34. Muñoz-Santiburcio, D. & Marx, D. Nanoconfinement in slit pores enhances water self-dissociation. *Phys. Rev. Lett.* **119**, 056002 (2017).
35. Zang, Y. et al. Flexible suspended gate organic thin-film transistors for ultra-sensitive pressure detection. *Nat. Commun.* **6**, 6269 (2015).
36. Gong, S. et al. A wearable and highly sensitive pressure sensor with ultrathin gold nanowires. *Nat. Commun.* **5**, 3132 (2014).
37. Huang, Y.-C. et al. Sensitive pressure sensors based on conductive microstructured air-gap gates and two-dimensional semiconductor transistors. *Nat. Electron.* **3**, 59–69 (2020).

Methods

Control of SVP

SVP was achieved by heating ultrapure water in a home-designed apparatus. Specifically, in a nitrogen-filled glovebox (<0.1 ppm oxygen), a large flat-bottomed beaker (volume, 500 ml; inner diameter, 121 mm; inner depth, 88 mm) filled with water was heated to a specific temperature with a hotplate to serve as a simple water bath. Subsequently, a polytetrafluoroethylene (PTFE) bottle (volume, 25 ml; inner diameter, 24 mm; inner depth, 52 mm) containing 4/5th ultrapure water (18.2 MΩ·cm) and with a hole (diameter, 1 cm) in the lid was placed in the water bath. To obtain as standard an SVP as possible, we made the liquid level of the water bath align with the height of the PTFE bottle as accurately as possible, but did not exceed the bottle height, which ensured that the liquid and vapour inside the PTFE bottle were at the same temperature. When the system reached stability at a certain temperature, the sample on the substrate was held over the hole in the PTFE bottle cap, which sealed the PTFE bottle and left the material in a saturated vapour state. Therefore, the required SVP can be precisely controlled by controlling the temperature of the external water bath. A schematic of the apparatus and more specific details can be seen in Extended Data Fig. 1.

Materials synthesis and water molecule adsorption

A variety of 2D materials were used in our experiments, including graphene, hBN, MoS_2, WS_2, ReS_2, WSe_2, $PdSe_2$, $PdTe_2$, PtS_2, etc., which were obtained by mechanically exfoliating the bulk crystals (purchased from HQ Graphene) and transferring them onto clean polydimethylsiloxane (PDMS) or SiO_2(300 nm)/P^+Si substrates. Gold films and P^+Si were also used in the experiments, and their preparation and transfer processes are described below. Note that to avoid unnecessary adsorption, all mechanical exfoliation and transfer processes were performed in a nitrogen-filled glov box.

To prepare a material for water molecule adsorption, the material was obtained and transferred to the PDMS; this creates a transfer stamp and facilitates the subsequent alignment transfer and lamination. Next, the SVP control apparatus was heated to a specific temperature (temperature range in the experiment, 40–100 °C) until the system was completely stable. Subsequently, the PDMS film with the material was installed over the hole in the PTFE, ensuring that the hole was completely sealed. In this way, different adsorption levels can be achieved precisely by presetting the evaporation temperature (that is, the water bath temperature) and thus varying the SVP. The molecular adsorption time of the material was controlled to 10 min to ensure the completion of natural adsorption at an SVP. The adsorption of all 2D materials and gold films was performed as described above, while P^+Si was adsorbed directly without transfer to PDMS.

Formation and control of vdW gaps

Briefly, the formation of the vdW gaps was accomplished by rapid lamination of the preabsorbed material onto another part by alignment transfer.

To create the vdW gap structure in 2D materials, in a nitrogen-filled glovebox, the preabsorbed subject 2D material on PDMS (at a specific SVP) was quickly mounted on a robotic arm of a transfer platform equipped with a microscope and subsequently mechanically aligned onto the second 2D material. The preabsorbed 2D material is thermally released from the PDMS by heating at 80 °C for 1 min, resulting in a vdW gap structure. The 1 min heating also ensured that some of the water islands on the surface of material can be tightly squeezed by the material to form an atomically flat water gap. Furthermore, once adsorption is complete, the preadsorbed material is physically contacted to another material as quickly as possible (typically <20 s) to minimize the natural evaporation of water molecules. vdW gaps of all heights are obtained by the process described above, changing only the SVP of the material adsorbed.

For the Au/gap/MoS_2 structure, gold films were obtained by predeposition on SiO_2/P^+Si substrates and polymethylmethacrylate-assisted exfoliation, as previously reported[38]. The film was subsequently transferred to PDMS to complete the water molecule adsorption and physically transferred to an MoS_2 layer to obtain the corresponding vdW gap structure using the previously described method.

For the Au/gap/P^+Si structure, to verify the feasibility of vdW gap engineering for a 3D/3D system, a method similar to that previously described was used here, but with the difference that water molecules were adsorbed on P^+Si, and another clean gold film was transferred to the silicon to form the vdW gap structure.

For the MoS_2/MoS_2 junction without a vdW water gap, the same PDMS-assisted transfer method was employed, simply without the adsorption of water molecules.

For the graphene/KI-gap/graphene and MoS_2/KI-gap/MoS_2 structures, KI solution (2–20 wt%) was used as an adsorption precursor instead of ultrapure water. The KI concentration for STEM analysis was 10 wt% (Fig. 3i,j). The same adsorption and assembly steps as before were employed and the layers were further assembled into vdW KI-gap structures.

For single-layer stacked gap structures, we used single-layer MoS_2 for adsorption and as the top material, assembled with a thick MoS_2 layer to form a gap structure in a similar way as previously described.

Device fabrication and measurement

MoS_2/gap/MoS_2 junctions were obtained using the preadsorption and assembly methods described above. Note that the thickness of two MoS_2 layers used here is ~7–10 nm, and to prevent the contact of the top/bottom MoS_2, a thin layer of hBN is used to cover the contact edge of the bottom MoS_2 for all devices to form a good sandwich structure (as illustrated in Fig. 4a). After that, electron-beam lithography was used to define electrode contacts with polymethylmethacrylate electron-beam resist (MicroChem). Metallization was achieved using thermal evaporation deposition of 10/50 nm Cr/Au with a deposition rate of 0.5 Å s^{-1} at ~10^{-5} torr. The lift-off process was further carried out in room temperature acetone. All electrical characterizations were conducted in a Lakeshore probe station in a vacuum environment (10^{-5}–10^{-6} torr) using semiconductor parameter analysers (Keysight B1500A and PDA FS-Pro). Note that pressure-sensing-related tests were performed in air using a computer-controlled speaker as the sound source for lower- and higher-frequency pressures. Here, we use a sound-level meter to measure the sound pressure level (in dB) generated by the speaker. The sound pressure P is defined as $P = P_0 10^{\frac{L_{dB}}{20}}$ in units of Pa, where P_0 = 20 μPa (reference sound pressure in air) and L_{dB} represents the measured sound pressure level.

Characterization

AFM characterizations were performed on a Bruker Dimension Icon system with a TESPA-V2 probe in a standard tipping model. Raman and PL measurements were conducted using a confocal Raman microscope (Witec alpha300R) under the excitation of a 488 nm laser. XPS (AXIS SUPRA) was used to characterize the MoS_2-related chemical composition and bonding information. Cross-sectional STEM slices of all samples were obtained with a Thermo Scientific Helios 5 CX FIB system. Specifically, a 1 μm protective layer is deposited in situ with platinum or carbon prior to ion beam bombardment of the sample, then the target region was etched using an accelerating voltage of 30 kV and a gallium ion beam of 2.8–47 nA to obtain a thick slice of the sample. The thick slice was then removed from the original substrate, placed on the STEM half-grid with a miniature robotic arm, and further thinned to <100 nm with a 24–790 pA gallium ion beam to form an ultrathin slice for STEM observation. All of the above steps were performed in a vacuum chamber of ~10^{-4}–10^{-5} torr. The STEM images (high-angle annular dark-field) and element mapping analyses of acquired sample slices were recorded on a Thermo Scientific Themis Z (3.2) microscope

equipped with a probe-forming aberration corrector at an operating voltage of 300 kV.

First-principles calculation

The DFT theory calculations were carried out by an open-source code Quantum ESPRESSO[39]. The Perdew–Burke–Ernzerhof exchange-correlation functional was used and the ultrasoft pseudopotentials were from the PSlibrary.1.0.0. The kinetic energy cut-offs for the plane-wave basis and charge density were 55 and 448 Ry. Basically, MoS_2 2 × 2 unit cells were used and the Brillouin zone *k*-point sampling at the ground-state calculation step was 3 × 3 × 1 where 3 × 3 are in-plane directions. The out-of-plane dimension was 5 nm to incorporate H_2O molecules and the dipole correction. Fermi–Dirac electron smearing was considered and the room-temperature parameters were assumed to capture the interlayer charge-transfer behaviour. In all the cases, crystal optimizations were adopted before ground-state calculations, with force and energy criteria of 1×10^{-4} Ry bohr^{-1} and 1×10^{-4} Ry, respectively. A dipole correction was also employed to restrain charge exchanges between adjacent image cells, which was realized by creating fictitious dipoles at the boundary of the out-of-plane dimension to keep the electrostatic potential flat.

Data availability

All the data generated and analysed in this study are included in the Article and its Supplementary Information. The data that support the plots within this paper and other findings of this study are available from the corresponding authors upon reasonable request.

References

38. Liu, Y. et al. Approaching the Schottky–Mott limit in van der Waals metal–semiconductor junctions. *Nature* **557**, 696–700 (2018).
39. Giannozzi, P. et al. QUANTUM ESPRESSO: a modular and open-source software project for quantum simulations of materials. *J. Phys. Condens. Matter* **21**, 395502 (2009).

Acknowledgements

This work was supported by the Strategic Priority Research Program of the Chinese Academy of Sciences (grant number XDB0580000), the National Key Research and Development Program of the Ministry of Science and Technology (grant numbers 2021YFA1200700, 2022YFB4400100), China National Funds for Distinguished Young Scientists Grant 61925403, China National Funds for Outstanding Young Scientists Grant 62122024, the China National Postdoctoral Program for Innovative Talents (grant number BX20230392), the Creative Research Groups Program of the National Natural Science Foundation of China (grant number 62321003), the National Natural Science Foundation of China (grant numbers 91964203, 62134001, 12174094, 62274060, 62311540157), the Natural Science Foundation of Hunan Province (grant numbers 2021RC5004, 2021JJ20028), the Guangdong Basic and Applied Basic Research Foundation–Regional Joint Fund (2020B1515120040), the Shenzhen Science and Technology Research Funding (JCYJ20200109115408041), the Key Research and Development Plan of Hunan Province (grant number 2022WK2001) and the Natural Science Foundation of Changsha (grant number kq2004002).

Author contributions

X.Z., L.L. and C.L. designed the research. C.L. prepared and characterized a series of vdW gap structures. C.L. and X.Z. performed device fabrication, electrical measurements and analysis. X.L., Y. Liu, C.M., K.L., Y.C. and J.H. participated in the experiment. Y. Lv conducted the DFT calculations and wrote the related discussions. C.L., X.Z, Y. Lv, L.L. and J.H. co-wrote the manuscript with inputs from all of the authors. All authors discussed the results and commented on the manuscript.

Competing interests

The authors declare no competing interests.

Additional information

Extended data is available for this paper at https://doi.org/10.1038/s41565-023-01579-w.

Supplementary information The online version contains supplementary material available at https://doi.org/10.1038/s41565-023-01579-w.

Correspondence and requests for materials should be addressed to Xuming Zou, Lei Liao or Jun He.

Peer review information *Nature Nanotechnology* thanks Simon Fleischmann and the other, anonymous, reviewer(s) for their contribution to the peer review of this work.

https://doi.org/10.1038/s41565-023-01579-w

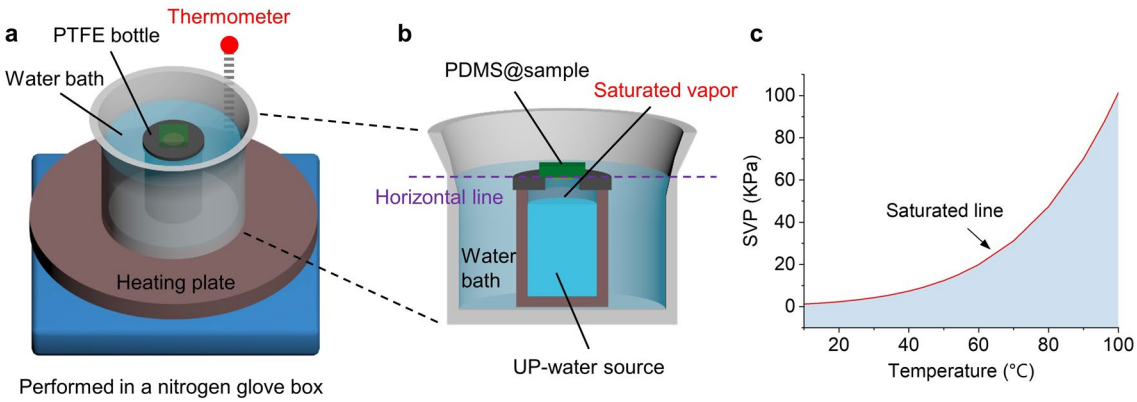

Extended Data Fig. 1 | Schematics depicting the generation and control of SVP. a, Schematic diagram of the SVP controlling apparatus. In the N_2-filled glove box, a PTFE bottle containing 4/5 UP-water with a hole in the top is heated by water bath. Since the experiments are performed in the glove box, the water bath is simply replaced by a beaker filled with water and a hot plate. **b**, Side view of the SVP generation apparatus. The horizontal line of the water bath is as close as possible to the top of the PTFE bottle to ensure that the gas and liquid inside the PTFE bottle are at the same temperature. When the system reaches stability at a specific temperature, the sample on the substrate (PDMS substrate) is fixed to the hole in the PTFE cap. At the same time, the PTFE bottle is sealed and the material underneath is in a saturated vapor state. Therefore, the required SVP can be precisely controlled by controlling the temperature of water bath. **c**, The correspondence between SVP and temperature. The SVP at different temperature can be calculated using the Antoni equation: $lg^P = A - (B/(t + C))$, here, P represents the SVP in kPa, t represents the temperature of the liquid in °C, and A, B and C are constants. For UP-water, the values of A, B, and C are 7.07, 1657.46 and 227.02, respectively.

https://doi.org/10.1038/s41565-023-01579-w

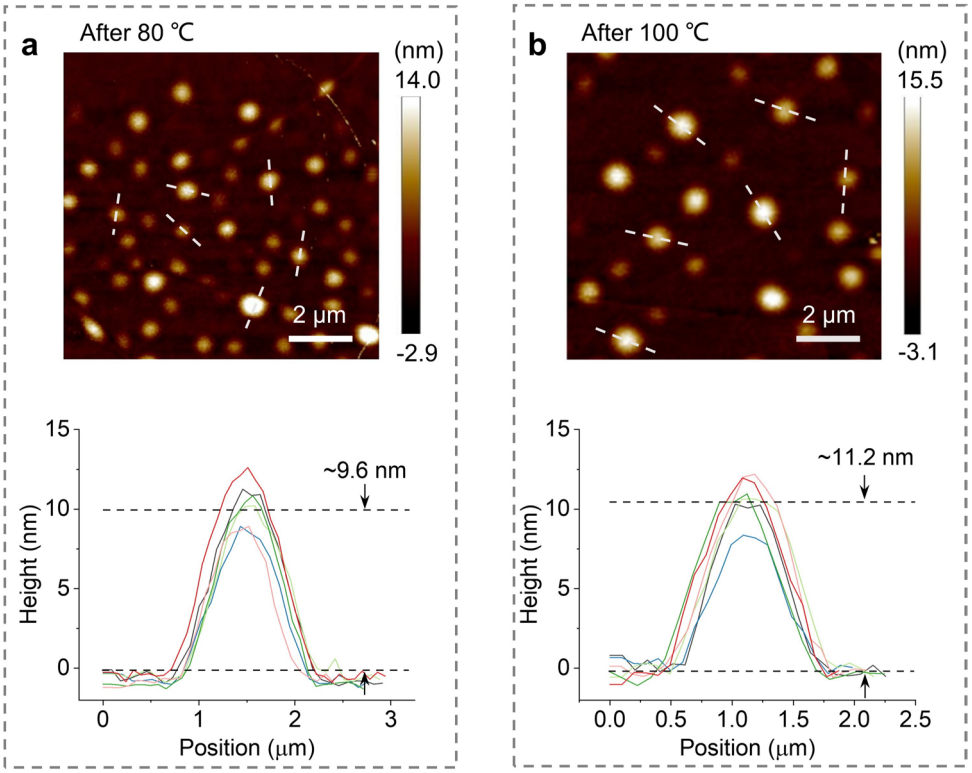

Extended Data Fig. 2 | Dynamic evolution of water molecule adsorption at 80 °C and 100 °C. a,b, AFM images of MoS_2 surface after at 80 °C for 10 mins (**a**) and 100 °C for 10 mins (**b**). Below: height profiles corresponding to the water islands on the AFM images, here the heights of water islands increase with temperature, indicating the feasibility of SVP to control the adsorption level.

https://doi.org/10.1038/s41565-023-01579-w

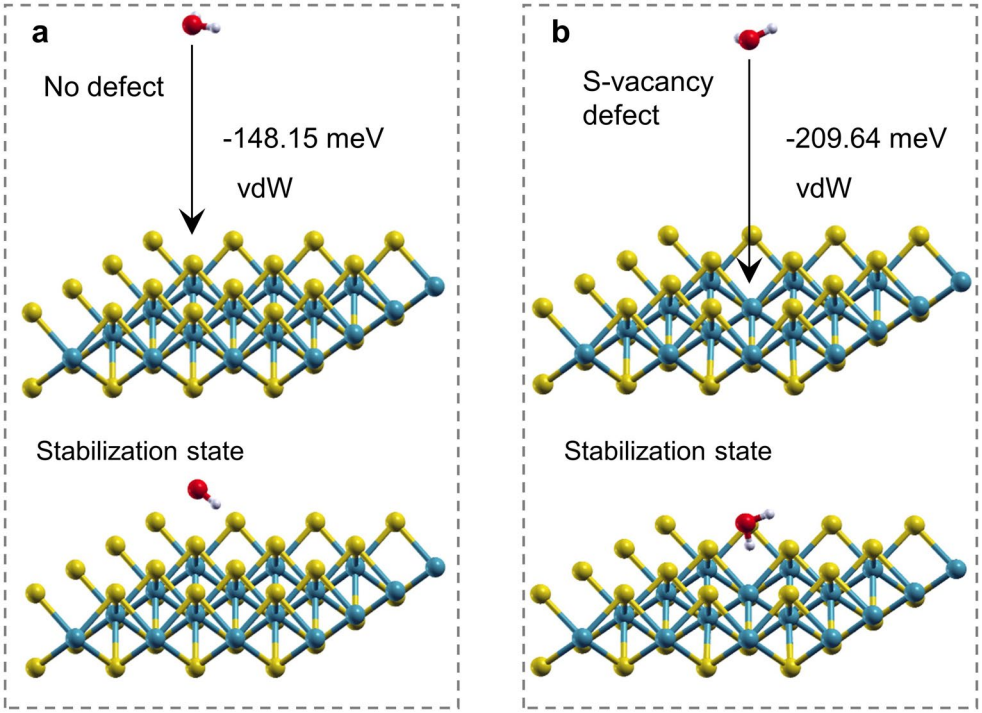

Extended Data Fig. 3 | The calculated vdW energy between water molecule and MoS_2 by DFT. a, Water molecule on defect-free MoS_2 surface. **b**, Water molecule on defective MoS_2 surface (missing an S atom).

https://doi.org/10.1038/s41565-023-01579-w

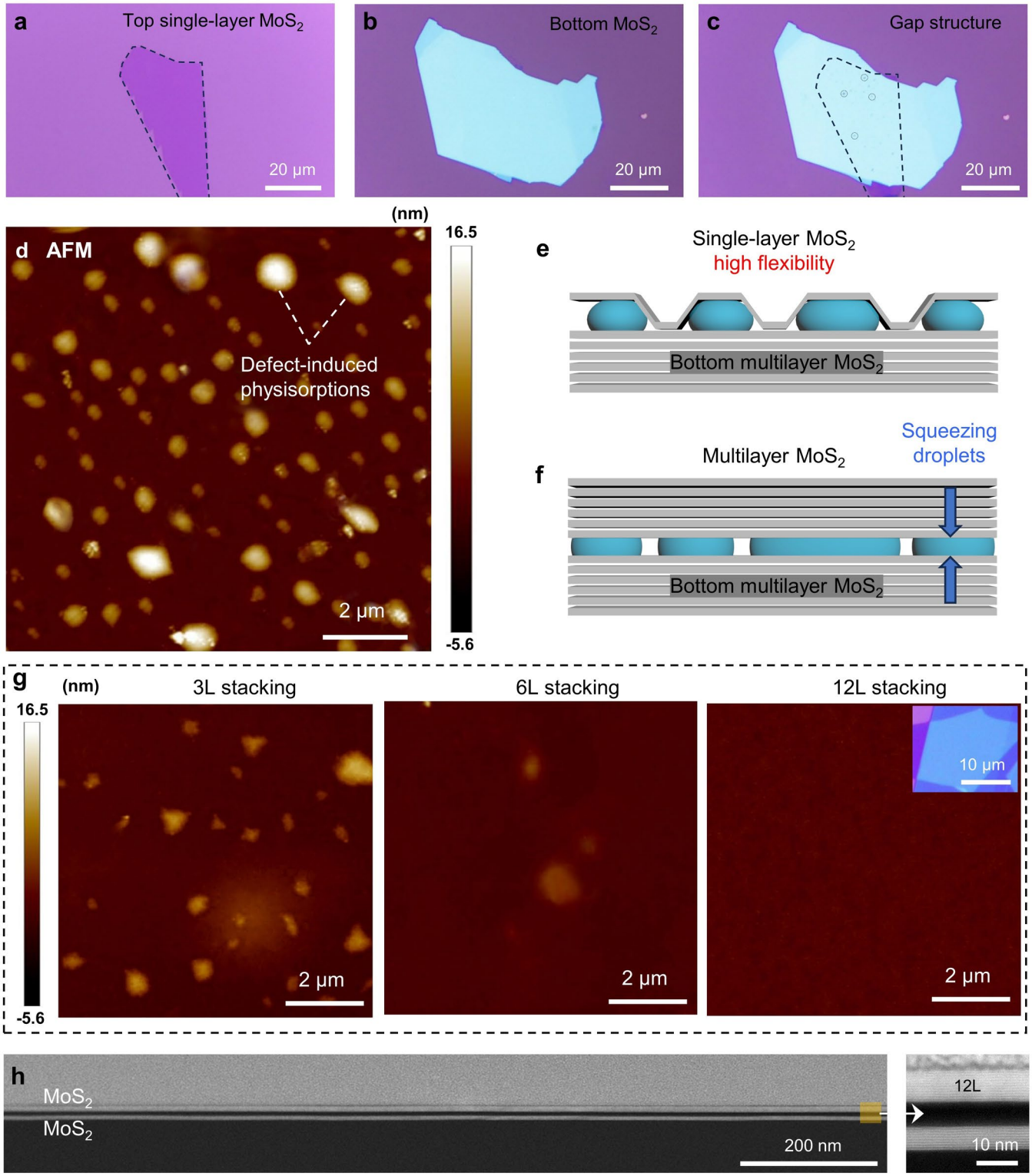

Extended Data Fig. 4 | Single-layer and multilayer MoS_2 stacked gap structures and related analysis. a-c, Optical micrographs of top single-layer MoS_2 (**a**), bottom multilayer MoS_2 (**b**) and vdW gap structure (**c**) assembled at T_{eva} = 100 °C. **d**, AFM image of the surface of single-layer gap structure, where a large number of water droplets are confined and visible due to the high flexibility of the single-layer MoS_2. **e**,**f** Schematic of the single-layer (**e**) and multilayer (**f**) MoS_2 gap structure. **g**, The surface AFM images of different thickness stacking, including the 3-layer, 6-layer and 12-layer MoS_2, showing that multilayer stacking is able to form flat surfaces due to the hardness of the multilayer material. **h**, Low magnification STEM image of the top 12-layer MoS_2 gap structure, showing that multilayer stacking is capable of creating large-sized and atomically flat gaps.

https://doi.org/10.1038/s41565-023-01579-w

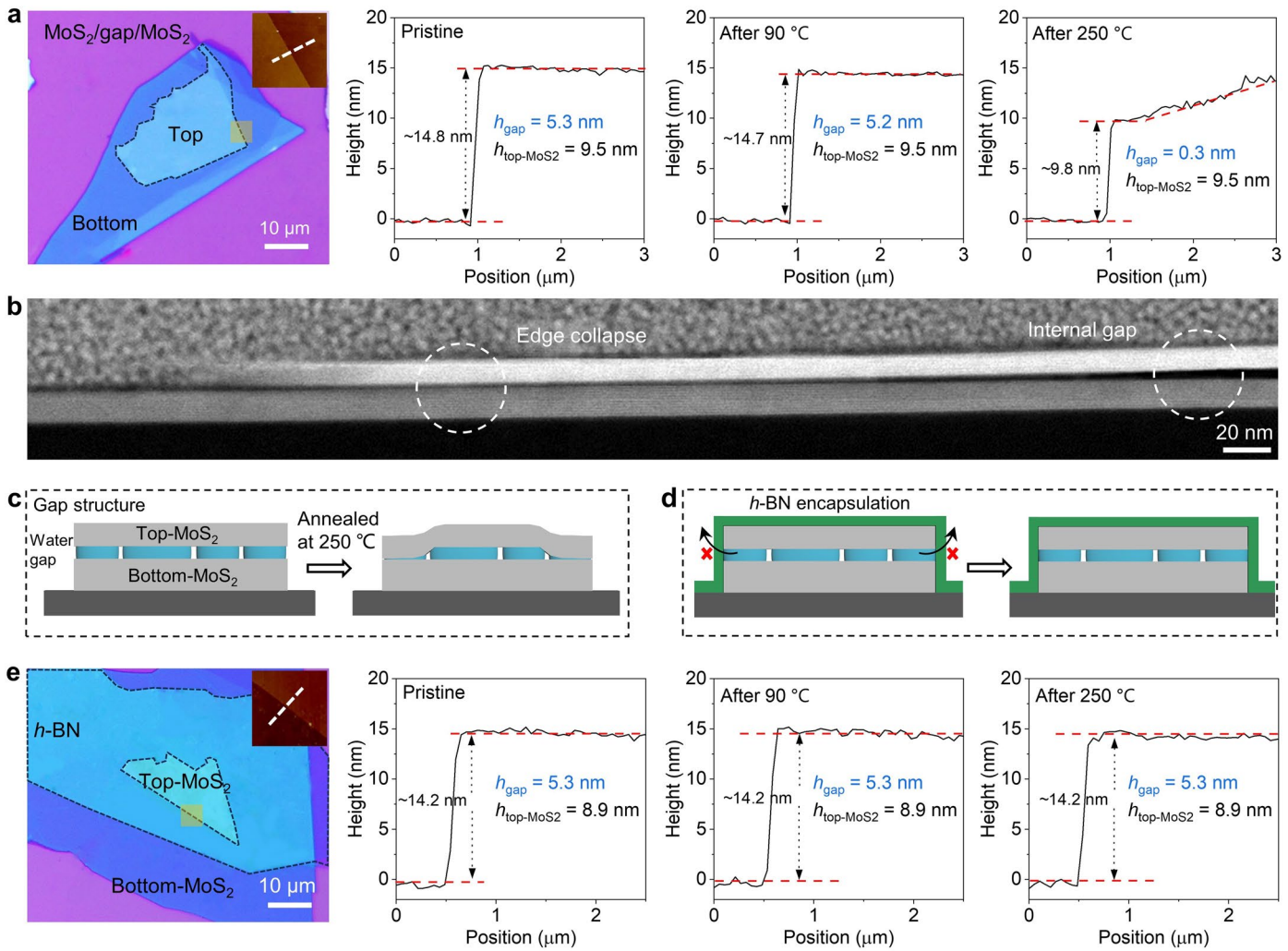

Extended Data Fig. 5 | AFM and STEM studies to demonstrate thermal stability of gap structures. a, Edge information of gap structures (assembled at T_{eva} = 100 °C) traced by AFM at different annealing temperatures. Below 90 °C, the water gap can be maintained, while at 250 °C, the edge of the gap completely collapses. **b**, STEM image of a gap structure with collapsed edges due to high temperature annealing. **c**, Schematic illustration of the edge collapse process of a gap structure. **d**, Schematic demonstrating the high temperature stability of an *h*-BN pre-packaged gap structure. **e**, Height variations in the *h*-BN pre-packaged gap structure traced with AFM, and here the pre-packaged gap structure is able to remain structurally stable even at 250 °C annealing. The yellow shading in (**a**,**e**) defines the AFM scan region (in the corresponding inset).

https://doi.org/10.1038/s41565-023-01579-w

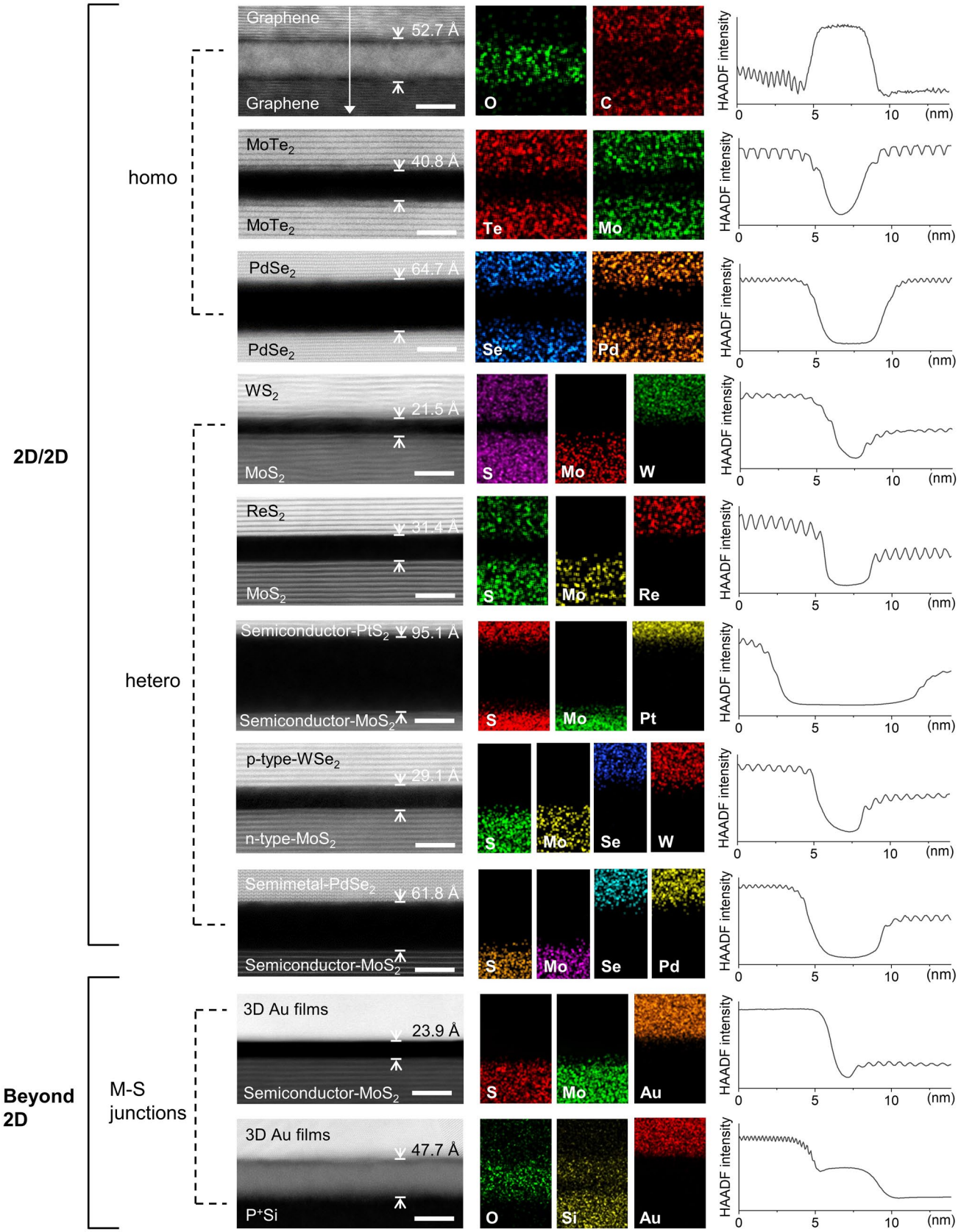

Extended Data Fig. 6 | The vdW gap structure of diverse building blocks and dimensions prepared by vdW gap engineering. We show that vdW gap engineering is able to be applied to different materials and different dimensions, including 2D/2D homojunction (such as Graphene/Graphene, $PdSe_2/PdSe_2$, and $MoTe_2/MoTe_2$), 2D/2D heterojunctions including p–n junctions and semimetal-semiconductor junctions (such as WS_2/MoS_2, PtS_2/MoS_2, ReS_2/MoS_2, WSe_2/MoS_2 and $PdSe_2/MoS_2$), even beyond 2D system including 2D/3D and 3D/3D metal-semiconductor junctions (such as Au/MoS_2 and Au/P^+Si). The M-S junctions are defined as metal/semiconductor junctions. All the scale bars, 5 nm.

https://doi.org/10.1038/s41565-023-01579-w

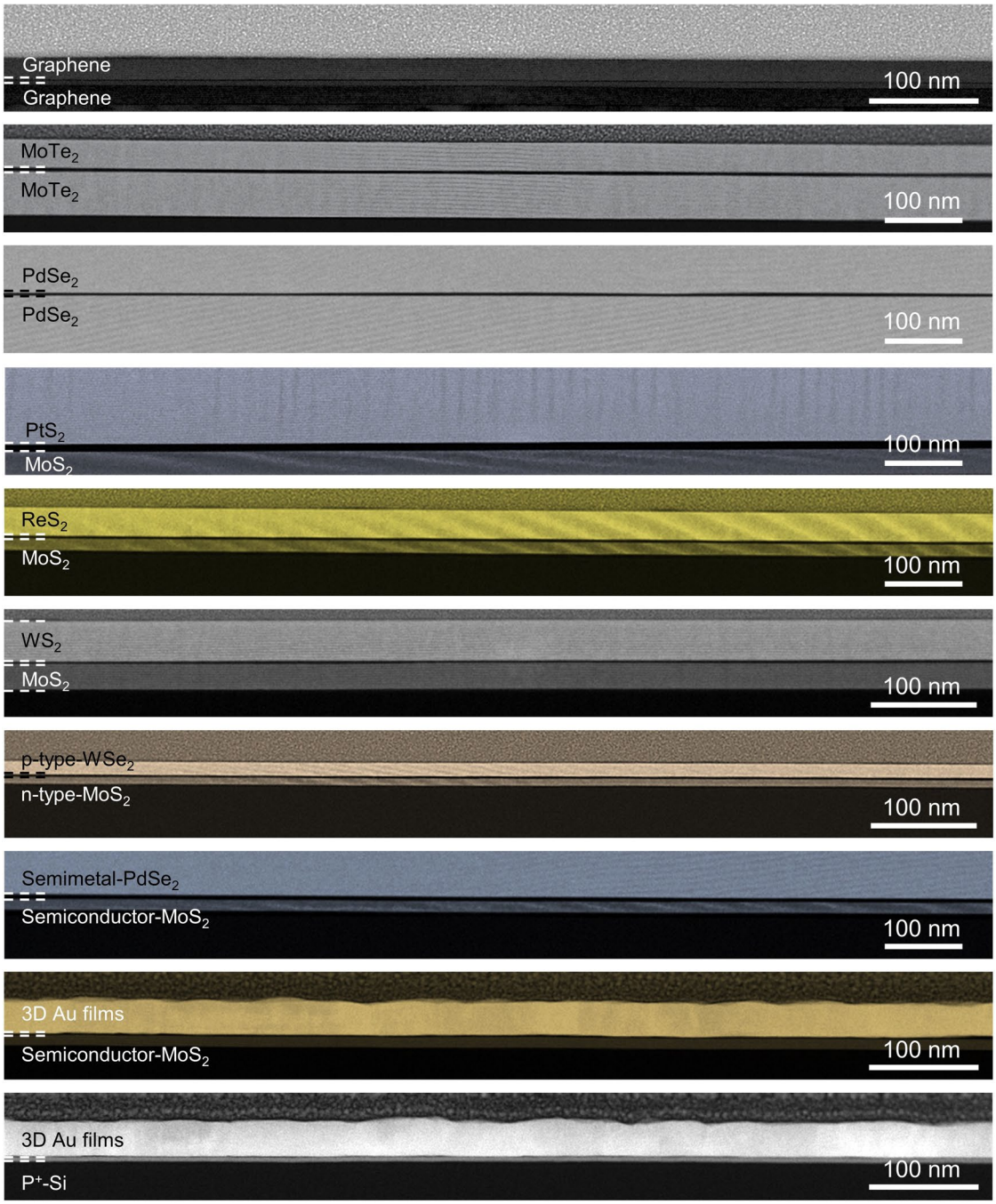

Extended Data Fig. 7 | Low-magnification STEM images to demonstrate the homogeneity of the vdW gaps. Here, all obtained vdW gap structures can be highly consistent over the micrometer length range.

https://doi.org/10.1038/s41565-023-01579-w

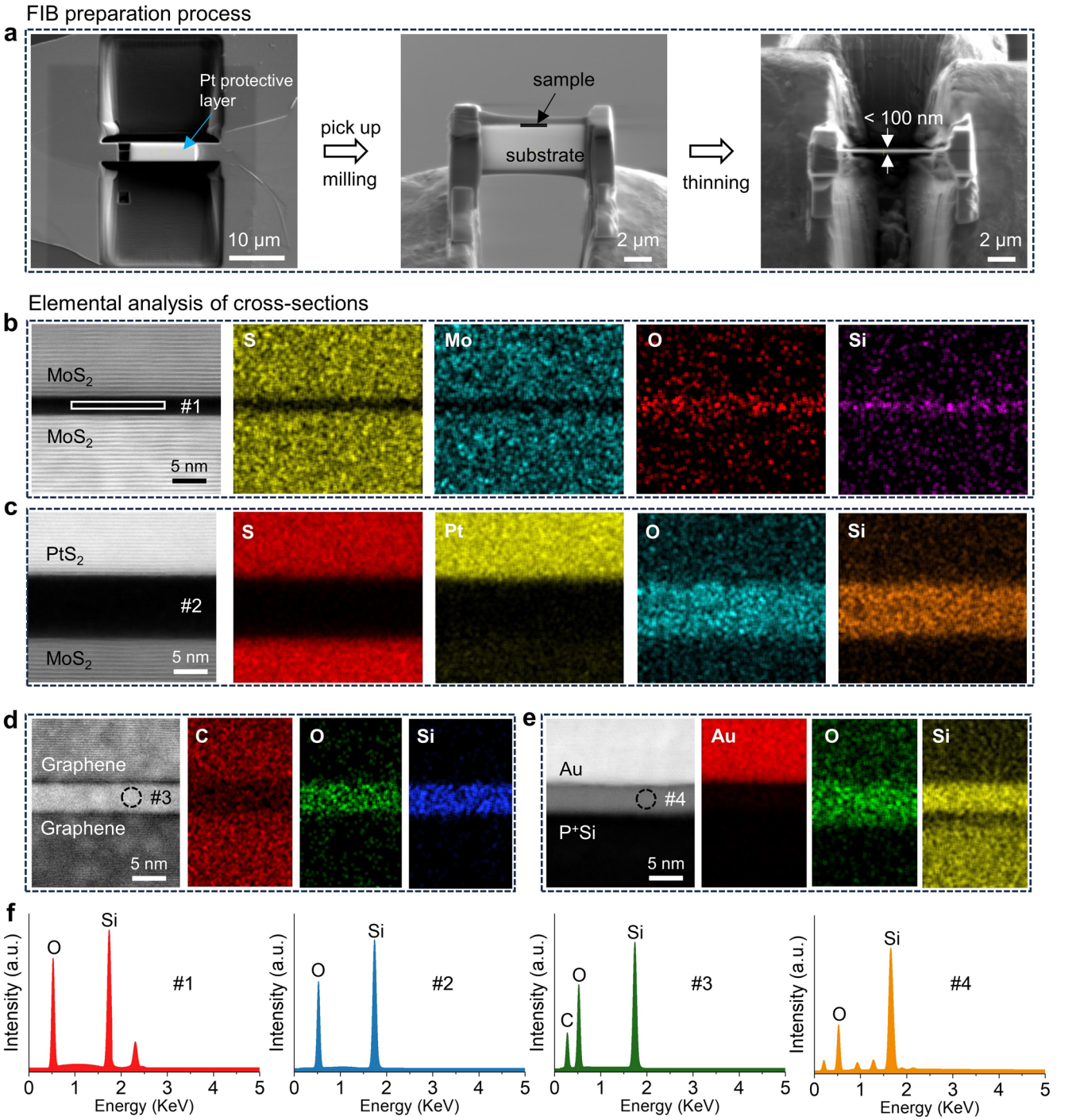

Extended Data Fig. 8 | Elemental analysis of gaps in cross-sections prepared by FIB. a, FIB process for preparing cross-sectional slices. The slices are ultimately thinned to less than 100 nm for subsequent STEM observations. **b**,**c**, EDS elemental maps of the cross-sections of a MoS_2/gap/MoS_2 structure (**b**) and a PtS_2/gap/MoS_2 structure (**c**), where a significant amount of Si elements are found in the gaps in both structures. **d**, STEM image and elemental analysis of a Graphene/gap/Graphene structure, where the re-deposited amorphous-Si in the gap can be directly seen due to the close Z-contrast (related to atomic-number) of C and Si (in HAADF-STEM). **e**, STEM image and elemental analysis of a P^+Si/gap/Au structure, here, the re-deposited Si in the gap can also be seen. **f**, EDS energy spectra corresponding to the four gaps above.

https://doi.org/10.1038/s41565-023-01579-w

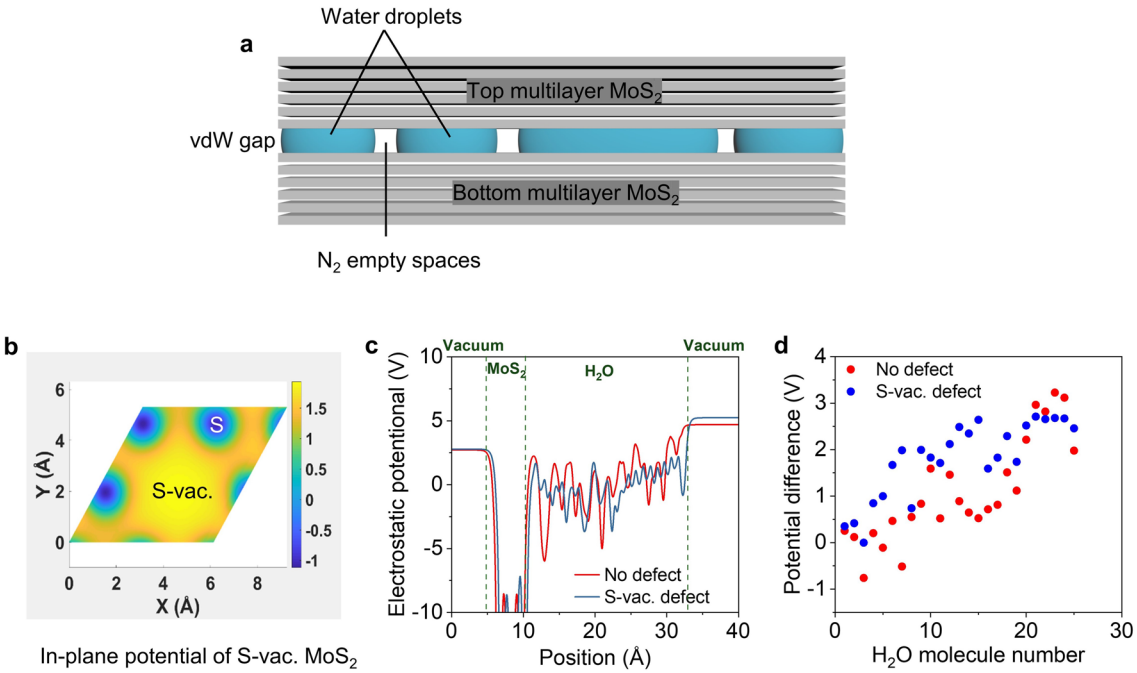

Extended Data Fig. 9 | Schematics related to droplet gap structure and transport, as well as polarization analysis of defect sites. a, Schematic explaining the water droplet gap, where the gap is alternately filled with N_2 and water droplets. **b**, The 2 × 2 MoS_2 supercell model and the in-x-y-plane potential on its top where an S vacancy (S-vac.) exists. **c**, Variation of polarization potential of water molecules on MoS_2 surface without and with S-vacancy defects calculated by DFT. **d**, Polarization-potential-difference in the vertical direction of the MoS_2/H_2O model without and with S-vac. defects.

https://doi.org/10.1038/s41565-023-01579-w

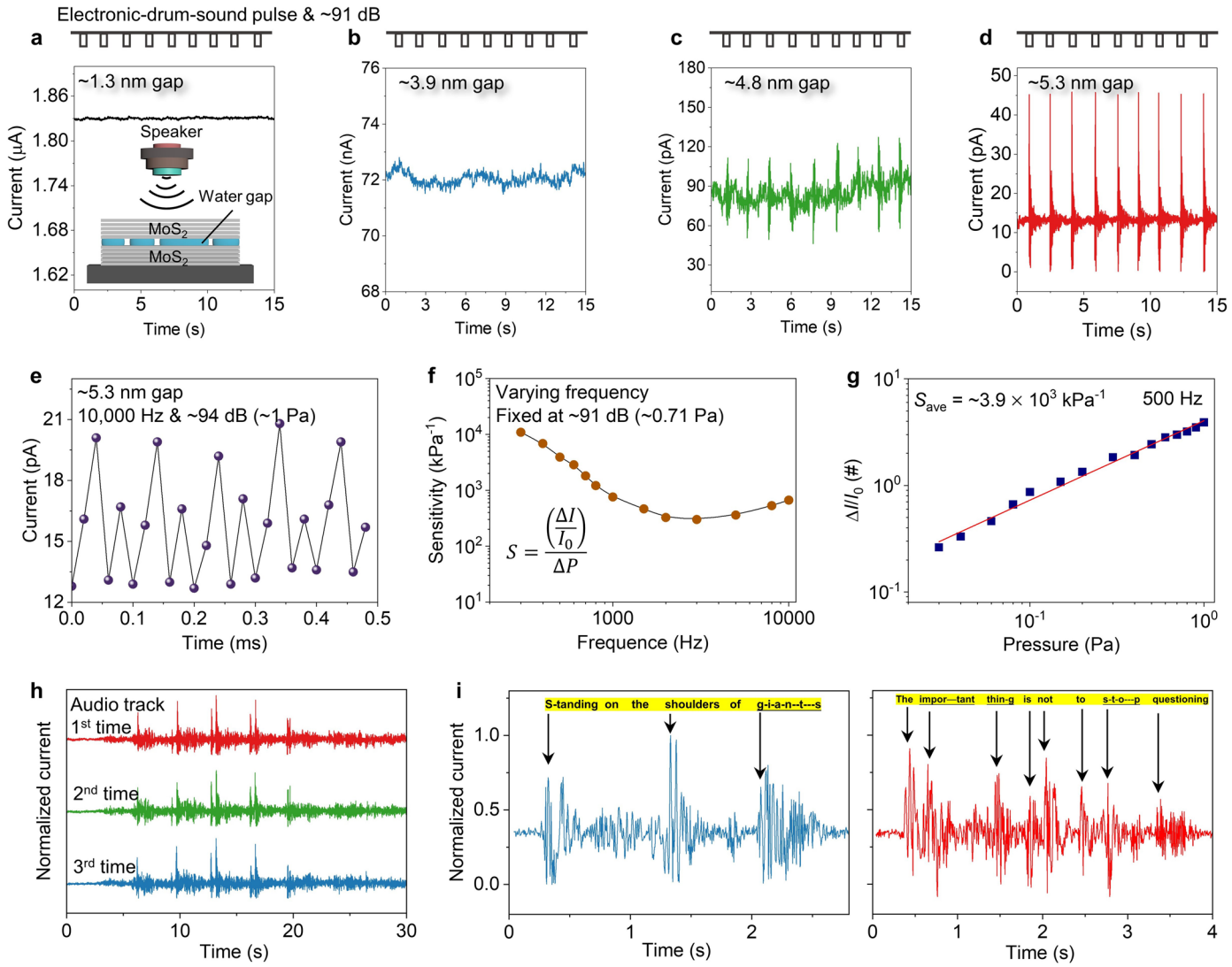

Extended Data Fig. 10 | MoS_2/gap/MoS_2 diodes for pressure sensing. **a**-**d**, Sound response characteristics of MoS_2/gap/MoS_2 diodes with different gap height at the voltage of −1 V, including ~1.3 nm gap (**a**), ~3.9 nm gap (**b**), ~4.8 nm gap (**c**) and ~5.3 nm gap (**d**). Inset of (**a**): schematic of MoS_2/gap/MoS_2 structure for pressure sensing test, and a computer-controlled speaker served as an acoustic source instead of the z-motor for obtaining smaller and higher frequency pressures. For a continuous steady electronic-drum-sound pulse (~91 dB), device with maximum gap height (~5.3 nm) shows the most significant and stable response. **e**, Current response of ~5.3 nm gap device for specific 10 kHz sound waves (~94 dB), highlighting the fast response of our devices (<25 μs, limited by our measurement set-up). **f**, Pressure sensitivity to the acoustic wave with different frequencies (300–10,000 Hz). **g**, Pressure response in ultralow pressure range (<1 Pa). Here, the device is consistently sensitive to different pressures with an average sensitivity S_{ave} of ~3.9×10^3 kPa^{-1}. **h**, Repeated test on musical sound waves, demonstrating the stability of the device under rapidly changing pressure. **i**, Discrimination of human speech sounds, for example, "Standing on the shoulders of giants" and "The important thing is not to stop questioning".